

# Availability analysis of a ship-to-ground FSO link

AIRTON F. G. JÚNIOR,<sup>1</sup>  CLAISSO P. AZZOLIN,<sup>1</sup>  CLAUDIO A. R. CASTILLO,<sup>2</sup>  AND VÍTOR G. A. CARNEIRO<sup>1,\*</sup> 

<sup>1</sup>Department of Defense Engineering, Military Institute of Engineering, Rio de Janeiro, RJ, Brazil

<sup>2</sup>Federal University of Rio de Janeiro, Rio de Janeiro, RJ, Brazil

\*Corresponding author: andrez@ime.eb.br

Received 3 August 2021; revised 28 December 2021; accepted 1 March 2022; published 30 March 2022

**This paper analyzes the availability of a free-space optical (FSO) communication link, established between a maritime platform and a land base. In this analysis, the impact of the laser beam misalignment, caused by the vessel's six oscillatory motions in a seaway, is considered. The hydrodynamic system is modeled, through a ship's response amplitude operator (RAO), under a typical sea-state condition. Finally, the link availability is calculated based on FSO losses, considering a beam with Gaussian power distribution.** © 2022 Optical Society of America

<https://doi.org/10.1364/JOCN.439148>

## 1. INTRODUCTION

In the context of mobile communications, either military or civilian, free-space optical (FSO) links present some potential advantages over radio frequency communications [1]. Due to FSO's high bandwidth, it is possible to transmit a significantly greater amount of information by means of an extremely directional optical beam, thus hindering the possibility of detection and intentional interference in the transmitted signal [2]. FSO systems are easily deployable and can be reinstalled without the cost of a dedicated fiber-optic cable. They are also capable of satisfying even the most demanding throughput requirements of today's high-definition television (HDTV) broadcasting applications [3].

Despite these advantages, the propagation of optical waves in free space is highly susceptible to atmospheric effects, such as absorption and spreading by molecules and aerosols, especially during rain or fog [4]. In addition, atmospheric turbulence has a strong impact on the availability of FSO links, generating effects such as scintillation, beam wander, and beam spreading [5]. Many studies have been carried out to reduce these effects, as well as enable the implementation of FSO on mobile platforms. In this context, the Naval Research Laboratory (NRL) conducted a high-availability communications test during a military exercise in the regions of San Diego and Honolulu, where FSO links were established between U.S. Navy ships [6,7]. Other studies have been developed aiming to make possible the use of FSO systems on high-speed trains (HSTs) [8–11].

One of the main concerns in all of these studies is pointing, acquisition, and tracking (PAT), which represents a great challenge to the consolidation of these communication systems [12]. Pointing errors can arise from vibrations of the equipment base, motions of mobile platforms, failures in the

tracking system, or boresight errors, which are fixed displacements between beam and receiver centers [13,14]. Hence, they can degrade the availability of the system and even interrupt the link [15,16].

The availability of terrestrial FSO links is a subject that has been heavily studied. In [17], an assessment of the availability rate of FSO and FSO/RF hybrid systems was carried out, considering the effects of atmospheric attenuation, and in [18], losses caused by the phenomenon of atmospheric turbulence were considered, with modeling based on the theory of Rytov's scintillation. In [19], an estimate was made of the availability of FSO links based on attenuations caused by fog, and in [20], the authors considered the impacts caused by rain in a country with a tropical climate. This performance parameter was also analyzed on other platforms, such as an airborne link, but considering the influence of losses caused by a generalized misalignment [21].

The use of FSO in vessels brings great challenges. Even if the vessel is anchored, the forces and moments of ocean waves cause translational and angular deviations in the transmitted optical beam. The setting proposed in this article is the following: an FSO transceiver (TX) is installed on a ship anchored at a position close to the coast; meanwhile, the receiver (RX) is fixed in a mast positioned on the beach (see Fig. 1). Due to its placement, TX is under the influence of the motions caused by the interaction of the ship with the ocean waves. It is also considered that the bow of the ship is, on average, pointed towards the beach in a position perpendicular to the coast.

Taking this scenario into consideration, this study analyzes the influence of the ship's wave-induced motions on the behavior of the communications system. In this sense, geometric, atmospheric, scintillation, and misalignment losses are calculated, considering that the optical beam is circular with Gaussian power distribution. Hence, this article aims to

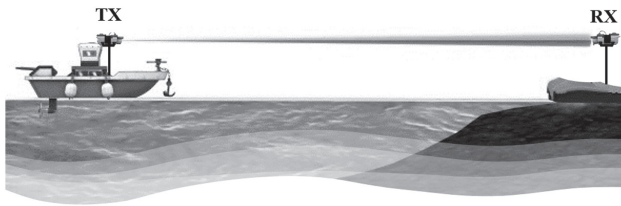


Fig. 1. Maritime FSO communication link.

analyze the availability of a maritime FSO communication link, considering the influence of the ship's translational and angular motions.

To this purpose, Section 2 shows some aspects related to the system modeling. Both hydrodynamic and FSO subsystems are presented in this section. The results are discussed in Section 3. Finally, the conclusions are presented in Section 4.

## 2. SYSTEM MODELING

For the sake of simplicity, the present study was divided into two main subsystems: hydrodynamic and optical. The flowchart of Fig. 2 shows the steps involved in modeling the two problems.

In general, the solution to the hydrodynamic problem consists of calculating the ship motions that influence the alignment of the FSO link. In this modeling, the hydrodynamic subsystem receives as input the parameters of a given sea state and provides as output the time series of motions that act at the base of the FSO transmitter. The transfer functions that establish a relationship between the inputs and outputs of this system are known as the response amplitude operator (RAO). The ship's RAO curves have a direct influence on the availability of the optical communication system.

The behavior of the sea is characterized by three parameters:  $H_s$ ,  $T_p$ , and  $\chi$ . The FSO subsystem is described by the parameters  $\theta$ ,  $L$ ,  $P_{TX}$ ,  $d_t$ ,  $d_r$ , and  $S_r$ . The performance analysis

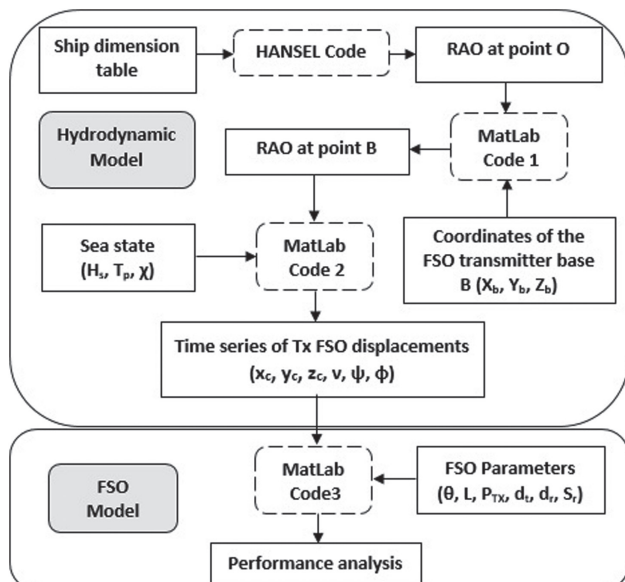


Fig. 2. Flowchart with the steps involved in modeling the maritime FSO communication link.

is based on the availability of the optical link. The meaning of these variables will be introduced in the next subsections.

### A. Hydrodynamic Subsystem

#### 1. Input Parameters

As previously stated, the hydrodynamic model receives three parameters that describe the behavior of the sea in the ship's anchoring position. This description uses statistical parameters such as significant wave height ( $H_s$ ) and peak period ( $T_p$ ) of the sea spectrum.  $H_s$  is the average wave height of the highest one-third of the waves, taken from a time-series record of a given sea state, while  $T_p$  is the period of maximum energy observed in the sea spectrum [22–24].

Based on these definitions, it is possible to evaluate, through the wave scatter diagram, the occurrence probability of a given sea state for a specific ocean region. This diagram relates the number of occurrences of the pairs ( $H_s$ ,  $T_p$ ) to the total number of ocean waves, observed for several years in the geographic region of interest. Table 1 shows the annual mean wave scatter diagram for area 11-32 (southeast coast of Brazil), averaged over 10 years of numerical weather prediction by the National Maritime Research Institute [25]. In Table 1, class intervals of  $H_s$  and  $T_p$  have been defined to count the occurrences. In order to specify one single value to represent each interval, the middle point within each range was used.

Thus, the representative values of pairs ( $H_{srp}$ ,  $T_{prp}$ ) were used as input parameters for the mathematical description of the sea behavior in the region where the ship operates. This mathematical description, also known as the JONSWAP spectrum [26], is commonly used in the analyses of ocean systems operating on the coast [27,28].

The wave incidence angle ( $\chi$ ), illustrated in Fig. 3, is another important parameter used to define the ship's behavior at sea. It characterizes the main direction of wave propagation, relative to the ship heading, and its value is equal to the opening angle measured counterclockwise from the ship's bow [29].

In this study, the influence of four wave incidence angles ( $0^\circ$ ,  $90^\circ$ ,  $135^\circ$ , and  $180^\circ$ ) that affect the vessel's hull was considered. Since the bow of the ship is, on average, pointing to the beach, the incidence of  $\chi = 0^\circ$  (stern sea) will predominate.

#### 2. Ship Transfer Functions

The ship used in this study is the U.S. Navy Ship (USNS) American Mariner, which was commissioned by the North American Armed Forces. Its main characteristics are summarized in Table 2. This ship was chosen due to its military characteristics and open access to information related to its hull geometry [30].

The output variables of the hydrodynamic subsystem were obtained by analyzing the sea influence on the ship. When the ocean waves encounter the ship's hull, the vessel develops translational motions along the  $X$ ,  $Y$ , and  $Z$  axes, called sway, heave, and surge, respectively. Angular motions are also observed around the axes of the body ( $x$ ,  $y$ ,  $z$ ), defined as pitch, yaw, and roll ( $v$ ,  $\psi$ ,  $\phi$ ), as represented in Fig. 3 [31]. It should be noted that the notation adopted for the axes follows the typical optical nomenclature, instead of the traditional

**Table 1. Wave Scatter Diagram for the Southeast Coast of Brazil**

$H_s$ (m)	$T_p$ (s)							TOTAL
	2-4	4-6	6-8	8-10	10-12	12-14	14-16	
7.5-8.0					0.00034			0.00034
7.0-7.5					0.00159	0.00007		0.00166
6.5-7.0					0.00166	0.00112		0.00278
6.0-6.5				0.00224	0.00621	0.00790		0.01635
5.5-6.0				0.01194	0.01387	0.02367	0.00027	0.04975
5.0-5.5			0.00024	0.03815	0.03812	0.05796	0.00217	0.13664
4.5-5.0			0.00465	0.08608	0.12399	0.10307	0.00648	0.32427
4.0-4.5			0.04158	0.23330	0.27094	0.19877	0.02486	0.76945
3.5-4.0			0.27556	0.43631	0.53609	0.41854	0.07214	1.73864
3.0-3.5		0.00020	1.08320	0.99051	1.06234	0.87540	0.12755	4.13920
2.5-3.0		0.01648	3.26143	2.21920	2.22171	1.74653	0.17707	9.64242
2.0-2.5		0.12999	6.51361	4.64552	4.86349	2.43795	0.14529	18.7359
1.5-2.0	0.00070	0.86601	9.01983	9.94359	6.97481	2.59206	0.10520	29.5022
1.0-1.5	0.00020	0.95463	7.32552	12.2426	5.35464	1.63160	0.06451	27.5737
0.5-1.0	0.00265	0.17910	2.10694	2.77194	0.97437	0.30666	0.00672	6.34838
0.0-0.5	0.86421	0.01184	0.04077	0.05738	0.03415	0.01038	0.00027	1.01900
TOTAL	0.86776	2.15825	29.6733	33.67876	22.4783	10.4117	0.73253	100.000

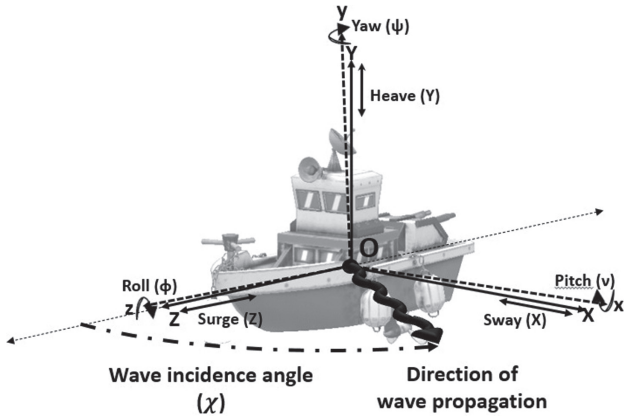


**Fig. 3.** Definition of ship's motions and wave incidence angle.

**Table 2. Main Characteristics of the Mariner Ship**

Parameter	Description	Value
$L_s$	Length	160.9 m
$W$	Beam (width)	23.1 m
$D$	Draft	9.068 m

hydrodynamics nomenclature, for the sake of compliance between the different areas of study.

In the classic study of the ship's behavior at sea, the floating body develops linear and harmonic motions relative to a point, whose average position is adopted as the origin of an inertial reference system [32]. When the ship is anchored, the forward speed is zero ( $U = 0$ ). Hence, this inertial system is fixed in space and coincides with the ship's average position. The origin of this system (point  $O$ ) is a Newtonian reference whose longitudinal position ( $ZG$ ), for the American Mariner, is located at 83.39 m after the ship's forward perpendicular (F.P.), as shown in Fig. 4. The vertical position ( $YG$ ) is on the line that indicates the ship's load waterline length (LWL), just

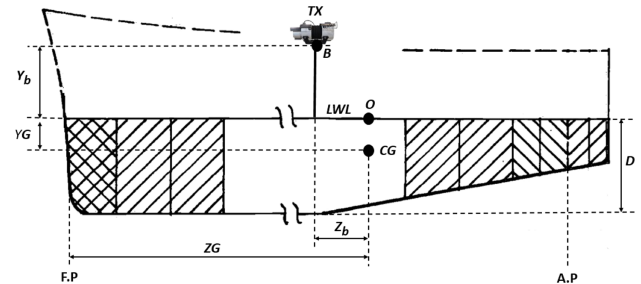


**Fig. 4.** Definition of the  $O$  point reference system.

90.5 cm above the vessel's center of gravity ( $CG$ ). The transverse position coincides with its centerline (diametrical plane), i.e.,  $XG = 0$  m.

In this study, the HANSEL program was used to calculate the RAO values for the six motions and four previously defined wave incidence angles [30]. HANSEL is a computational tool, based on linear potential theory in the frequency domain, used in seakeeping analysis. This program requires the vessel's underwater geometry to be input as offset points for several cross sections along the ship. The RAO values are associated with the inherent characteristics of the ship for a given loading condition, excitation period, and incidence angle, i.e., they represent the responses (amplitudes and phases) of the floating system to regular waves. Based on these parameters and knowledge of the characteristics of the sea state, it is possible to determine the displacements, speeds, and accelerations at any point of the ship's hull. The RAO is defined as [29]

$$RAO_i(\omega_e, \chi) = \frac{S_{ia}}{\zeta_a}, \tag{1}$$

where  $S_{ia}$  is the response amplitude of the  $i$ th degree of freedom and  $\zeta_a$  is the amplitude of the regular wave in meters. The amplitudes of the translational motions ( $i = 1, 2, 3$ ) are given in meters and those of the rotational motions ( $i = 4, 5, 6$ )

are in degrees.  $\omega_e$  is the encounter frequency, defined as the frequency at which the ship encounters the waves of frequency  $\omega_w$  [24]. In this work, since  $U = 0$ ,  $\omega_e = \omega_w$ .

Since HANSEL's output provides the responses at the ship's origin  $O$ , the translational motions at a generic point of the ship are obtained by a transformation of reference axes [24]. The rotational motions are always the same, independent of which point is being considered. In this way, it is possible to calculate the RAO values of the FSO TX absolute displacements, installed at point  $B$  ( $x_b = 0$  m,  $y_b = 20$  m,  $z_b = 10$  m).

### 3. Output Parameters

The response of a ship, under real sea conditions, can be determined by the linear superposition of each regular wave component that is used to model the real sea [33]. Hence, the motions in irregular waves are obtained by adding regular waves of different amplitudes, frequencies, and directions of propagation. Based on the wave energy spectrum and the frequency characteristics of the ship's RAOs, the response spectrum and statistics can be found [33]. The response spectrum,  $S_{ia}(\omega_e)$ , is obtained through [29]

$$S_{ia}(\omega_e) = S_e(\omega_e)[\text{RAO}_i(\omega_e, \chi)]^2, \quad (2)$$

where  $S_e(\omega_e)$  is the sea spectrum.

The proposed FSO system was simulated, positioned on the maritime platform presented in Fig. 4. The RAO values produced by HANSEL, were used in MATLAB Code 1 (see Fig. 2) to calculate the RAO spectrum at point  $B$ . This spectrum and the information related to the sea state ( $H_s$ ,  $T_p$ ,  $\chi$ ) were, subsequently, inserted into MATLAB Code 2, which implements Eq. (2) to obtain the Mariner's response spectrum, given the desired sea conditions.

Finally, in order to obtain the time series of the ship's motions at the point of interest (FSO TX), this second code used MATLAB's WAFO toolbox [34] to generate temporal records from the ship response spectrum. This way, the time series for the six degrees of freedom were calculated for a time window of 20 min.

### B. Optical Subsystem

The time series of the motions at the FSO TX were used as input parameters to the optical subsystem. The availability of the FSO link was analyzed, considering a laser with Gaussian power distribution as the optical source. A Gaussian beam is a natural byproduct of the laser-forming process in a resonant cavity [35]. For this reason, lasers used in optical communications operate many times in the fundamental transverse electromagnetic mode (TEM<sub>00</sub>), which produces a Gaussian profile [36]. The optical intensity can be observed through the irradiance profile, given in cylindrical coordinates by [37]

$$I(\rho, \phi, z) = I_0^2 \frac{r_t^2}{r_L^2(z)} \exp \left[ -\frac{2\rho^2}{r_L^2(z)} \right], \quad (3)$$

where  $I_0$  is a constant related to power at the TX output,  $r_L(z) = r_t + \frac{\theta \cdot z}{2}$  is the beam width along  $z$ ,  $r_t$  is the TX scope radius, and  $\theta$  is the beam divergence angle.

The detected power is obtained by the integration of the irradiation profile over the surface of the receiver. In order to include the effects of radial misalignment, it is necessary to translate axes over Eq. (3). Using rectangular coordinates, the peak of the Gaussian beam can be translated by  $x_c$  and  $y_c$  away from the origin, representing translational motions of TX, while the center of RX remains on the origin. Hence, the power of the misaligned beam, at the receiver ( $Z = L$ ), is given by [38]

$$P_{RX} = \int_S I_0^2 \frac{r_t^2}{r_L^2} \exp \left[ -\frac{2[(x - x_c)^2 + (y - y_c)^2]}{r_L^2} \right] dS, \quad (4)$$

where  $S$  is the aperture area of the receiver.

Due to its availability gain in simulations of misaligned links, especially in moving systems, a recently proposed formulation was used for the combined geometric and radial misalignment attenuation, given in dB, by [38]

$$\alpha_{gm}[\text{dB}] = 10 \cdot \log_{10} \left[ 1 - Q_1 \left( \frac{2d}{r_L}, \frac{2r_r}{r_L} \right) \right], \quad (5)$$

where  $Q_1$  is the Marcum  $Q$ -function of order 1,  $d$  is the absolute radial misalignment, and  $r_r$  is the RX aperture radius.

Equation (5) can also be used to include angular misalignment between TX and RX, i.e., rotational motions. This way,  $\alpha_{gm}$  can be calculated approximating  $d$  by

$$d = \sqrt{[x_c + L \cdot \tan(\phi)]^2 + [y_c + L \cdot \tan(\nu)]^2}, \quad (6)$$

where  $\phi$  represents the yaw,  $\nu$  the pitch angle of rotation, and  $L$  the link distance. Regarding the other two motions,  $z_c$  was included as variations in  $L$ , and  $\psi$  was considered when making the hydrodynamic calculations of  $x_c$  and  $y_c$ .

Beside geometric and misalignment losses, scintillation was also considered. This effect is caused by refractive index irregularities and, for its complete study, a statistical approach is necessary. However, several authors developed an attenuation coefficient due to scintillation, bringing a deterministic simplification to this statistical effect [5,39,40]. For this work, the effect of misalignment is considered to have a greater impact on the availability of the link than scintillation. Hence, a simplified model was used, based on Andrews's method [40].

Scintillation is usually described by the structural parameter of the refractive index,  $C_n^2$ , which represents the impact of the turbulence on the oscillation of optical power [5]. The parameter  $C_n^2$  can range from  $10^{-15}$  to  $10^{-12} \text{ m}^{-2/3}$ , which are characteristic values for weak and strong turbulences, respectively. In this work,  $C_n^2 = 10^{-14} \text{ m}^{-2/3}$  was chosen, which corresponds to a scintillation loss between 1 and 1.56 dB for the distances considered in the scenario of Fig. 1 [41].

Atmospheric attenuation is caused by the absorption and spreading of the light in the atmosphere components [42]. The proposed FSO system was designed to operate under conditions of clean weather and fine fog. This corresponds to an operational range of  $\alpha_{\text{atm}}$  between 1 and 2 dB/km.

Thus, the total loss on the FSO maritime link in dB is [43]:

$$\alpha_{\text{tot}}[\text{dB}] = \alpha_{gm} + \alpha_{\text{atm}} \cdot L + \alpha_{\text{scint}} + \alpha_T + \alpha_R, \quad (7)$$

where  $\alpha_{scint}$  is the loss due to scintillation, and  $\alpha_T$  and  $\alpha_R$  are the losses in the fiber–telescope interfaces of the transmitter and receiver, respectively. All losses are given in dB.

### C. Availability Analysis

Simulations were carried out to evaluate the influence of ship motions upon the availability of the FSO system. These analyses were developed based on the observation of the received power over time. This way, the system availability rate ( $\eta$ ) was calculated. In communications, the availability is usually expressed as a percentage of uptime in one year. Nevertheless, due to the periodic characteristic of maritime waves, a sequence of uptimes and downtimes is observed over a time scale of minutes, depending on the sea state.

Thus, the availability rate was obtained through the relation between uptime ( $t_{up}$ ) and total simulation time ( $t_T$ ), i.e.,

$$\eta = t_{up}/t_T = t(d < d_{max})/t_T, \tag{8}$$

where  $t_{up}$  is the time in which the received power ( $P_{RX}$ ) remains above the sensitivity level of the receiver ( $S_r$ ).

This rate can also be expressed by analyzing the behavior of the total link misalignment over time. In this context, we define  $d_{max}$  as the maximum admitted misalignment at which the power reaches the threshold ( $P_{RX} = S_r$ ). Thus, the availability rate is also given by the second part of Eq. (8).

## 3. SIMULATION, RESULTS, AND DISCUSSION

### A. Simulations of the Hydrodynamic Subsystem

During the seakeeping analysis in the frequency domain, 60 regular wave frequencies were considered. These frequencies correspond to the range of  $2\text{ s} < T < 28\text{ s}$  and were defined in a configuration file of input parameters in HANSEL. This data file was processed by HANSEL to obtain the values of the amplitudes and phases of the ship’s motions for the four different wave incidence angles. Based on these values, the Mariner’s RAO curves at point  $O$  were obtained. Figure 5 shows the RAO amplitudes for  $\chi = 0^\circ, 90^\circ, 135^\circ,$  and  $180^\circ$ .

The maximum amplitude of the translational motions (1.514 m/m) is observed for the heave motion at  $T = 7.748\text{ s}$ , when  $\chi = 90^\circ$ . For the rotational motions, the maximum

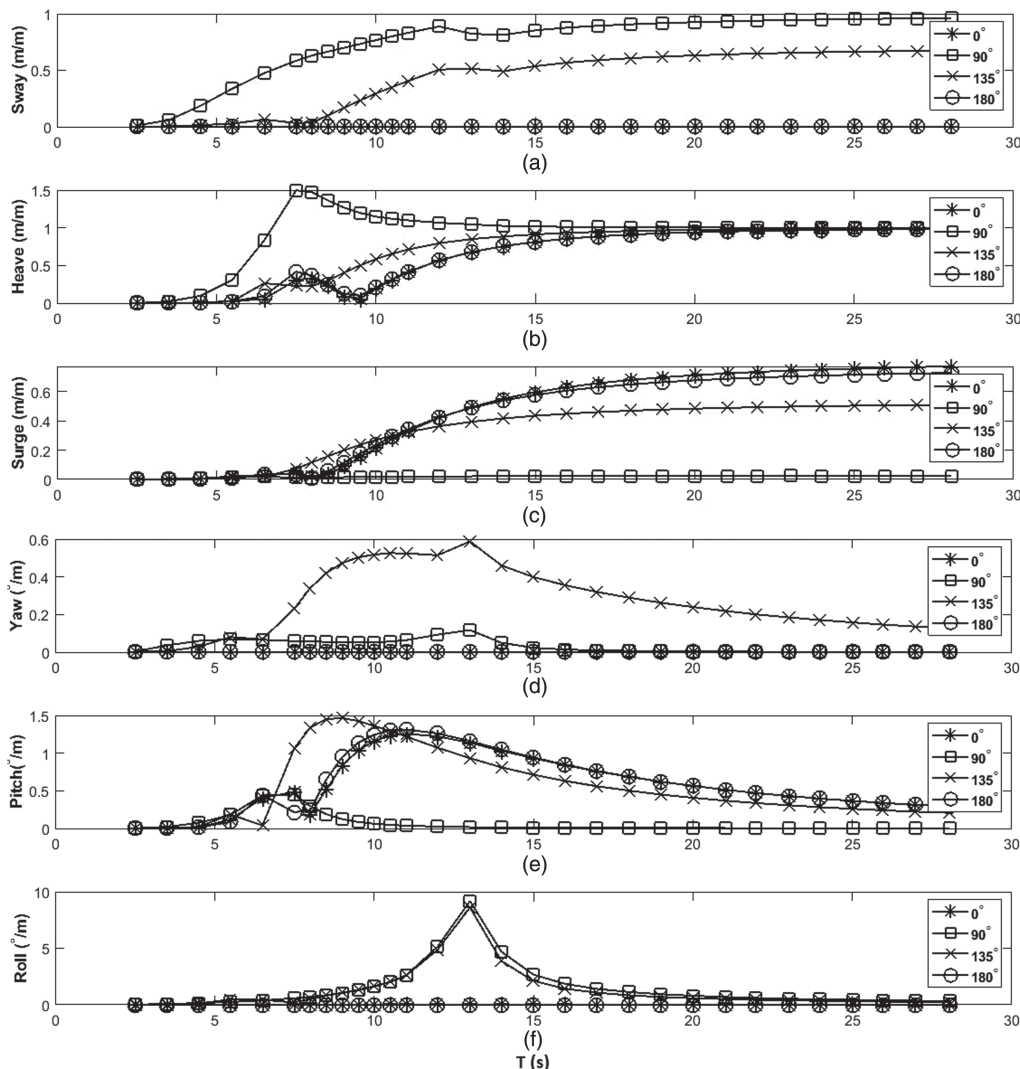
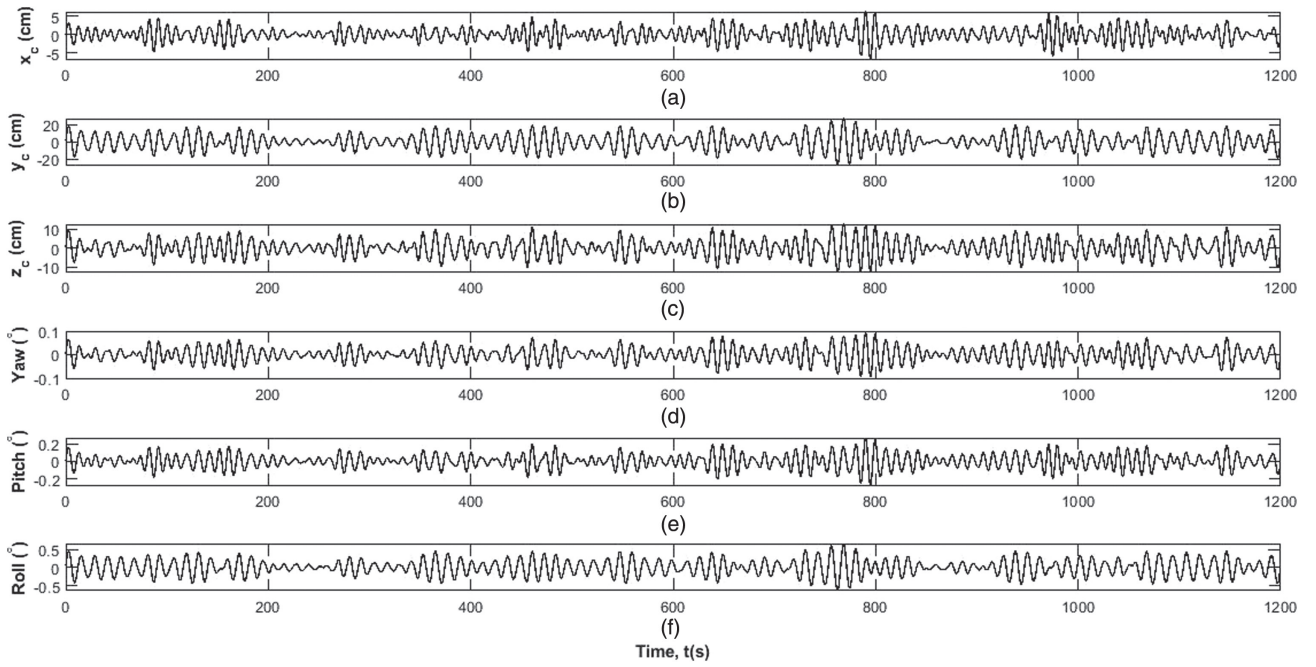


Fig. 5. RAO curves for the six motions at point  $O$ : (a) sway, (b) heave, (c) surge, (d) yaw, (e) pitch, and (f) roll.



**Fig. 6.** Time series of FSO TX displacements for the sea state ( $H_s = 0.25$  m,  $T_p = 11$  s,  $\chi = 135^\circ$ ).

amplitude ( $9.187^\circ/\text{m}$ ) is observed for roll at  $T = 13$  s, when  $\chi = 90^\circ$ . However, due to the FSO longitudinal transmission axis, pitch and yaw motions cause a higher impact, especially in their resonance points. This will be noted when the availability results are presented, as a low availability at  $T = 11$  s. Figure 5 also shows that the pitch motion produces two main resonances:  $1.256^\circ/\text{m}$  for ( $T = 11.51$  s,  $\chi = 180^\circ$ ) and  $1.514^\circ/\text{m}$  for ( $T = 7.747$  s,  $\chi = 135^\circ$ ). The yaw maximum value is  $0.588^\circ/\text{m}$  for ( $T = 12.49$  s,  $\chi = 135^\circ$ ).

The values of amplitude presented in Fig. 5 were used in MATLAB Code 1 (see Fig. 2) to calculate the RAO at point  $B$ . With this data and the sea spectrum, MATLAB Code 2 was used to calculate the motions that act at the base of the FSO TX, which are shown in the time series of Fig. 6. The sea state ( $H_s = 0.25$  m,  $T_p = 11$  s,  $\chi = 135^\circ$ ) was chosen to evaluate the impact of the yaw and pitch motions when the ship is in a resonant condition. This figure shows that the greater motions occurred for  $Y_p$  (heave) and roll motions.

Following the flowchart of Fig. 2, MATLAB Code 3 was used to obtain the optical availability for the four incidence angles and all pairs of representative values ( $H_s$ ,  $T_p$ ) of the scatter diagram (Table 1). However, for the sake of conciseness, we chose to show only the results for the sea state ( $H_s = 0.25$  m,  $T_p = 11$  s) and  $\chi = 135^\circ$ , the angle at which the vessel develops motions in all six degrees of freedom. The next subsection presents the optical results, used to obtain the availability. Whenever a time-domain analysis is shown, this resonant state was chosen.

## B. Simulations of the Optical Subsystem

This subsystem was simulated using the optical parameters presented in Table 3, which were based on typical values and

**Table 3.** Parameters of the FSO System

Parameter	Description	Value
$P_{TX}$	Laser power	14 dBm
$L$	Link length	3–5 km
$\alpha_{atm}$	Atmospheric loss	$\leq 2$ dB/km
$\alpha_T$	Insertion losses in transmitter	1 dB
$\alpha_R$	Insertion losses in receiver	1 dB
$\alpha_{scint}$	Scintillation loss	1–1.56 dB
$d_t$	FSO transmitter diameter	5 cm
$d_r$	FSO receiver diameter	20 cm
$\theta$	Divergence angle	1–3.5 mrad
$S_r$	FSO receiver sensitivity	–36 dBm
$\lambda$	Signal wavelength	1550 nm
$\lambda_b$	Beacon wavelength	785 nm
$R_b$	Data bit rate	1 Gbps

experimental data of FSO systems [1,12,16,44]. An operational range was defined for the scenario described in Fig. 1. Thus, the proposed FSO system must meet the length range and changes in atmospheric loss specified in Table 3. The scintillation loss depends on distance, so it is variable. The divergence angle was made variable to evaluate its influence.

The atmospheric loss range adopted in this work was based on the Malaysia KL model [20], which predicts a maximum atmospheric loss of 3 dB/km, for rain rates up to 10 mm/h, in a tropical climate. Besides, data collected in 2020 relating to rainfall rates in Rio de Janeiro show that the atmospheric attenuation is limited to 3 dB/km approximately 99.8% of the time (rain rates  $< 10$  mm/h) [45]. Hence, a conservative atmospheric loss up to 2 dB/km was adopted as the operational range so as to privilege the system availability, as explained later.

On one hand, FSO transceivers operating without an acquisition, tracking, and pointing (ATP) system usually have a

divergence angle of 2 to 10 mrad to compensate for the effects of platform motions. On the other hand, FSO systems that have an ATP mechanism can operate with a narrower divergence angle (0.05–1 mrad), thus increasing the system’s range [16]. In communications tests between U.S. naval ships conducted by the NRL, for example, the FSO transceivers were configured with ATP and  $\theta = 1$  mrad [1]. In the present study, we propose the use of a CW laser on another wavelength (see Table 3) as a beacon to signalize if the link is ready to transmit.

The optical subsystem is analyzed in terms of divergence angle, length, and atmospheric loss in the following subsections.

### 1. Divergence Angle

Initially, the received power was evaluated as a function of total misalignment for different divergence angles using  $L = 3$  km and  $\alpha_{\text{atm}} = 1$  dB/km. Considering a condition of perfect alignment ( $d = 0$  m), Fig. 7 shows the optical power decreasing due to the increase in the angle of divergence. This reduction is caused by the increase in geometric loss. We can also see that the power decreases as the total misalignment increases. Furthermore, higher beam divergences increase the maximum allowed misalignment ( $d_{\text{max}}$ ), making the FSO system less sensitive to the hydrodynamic motions. For example, at 3.5 and 4 mrad, the link is operational for  $d \leq 6.345$  and 6.792 m, respectively.

Other simulations were carried out for  $L = 3$  km and different values of  $\alpha_{\text{atm}}$ . Table 4 consolidates these results. As a general behavior, increasing the divergence angle up to 4 mrad, increases  $d_{\text{max}}$ , while increasing  $\alpha_{\text{atm}}$  up to 3 dB/km decreases  $d_{\text{max}}$ .

Figure 8 shows the results for  $L = 5$  km and  $\alpha_{\text{atm}} = 2$  dB/km. In comparison to Fig. 7, the increase of 2 km in  $L$  and 1 dB/km in  $\alpha_{\text{atm}}$  caused a reduction in  $d_{\text{max}}$  for the entire range of  $\theta$ . For example,  $d_{\text{max}}$  was reduced to 2.271 m for  $\theta = 3.5$  mrad, while the system becomes inoperative for  $\theta = 4$  mrad. Unfortunately, when further increasing  $\alpha_{\text{atm}}$ , the system only works for very small values of  $\theta$ , which implies

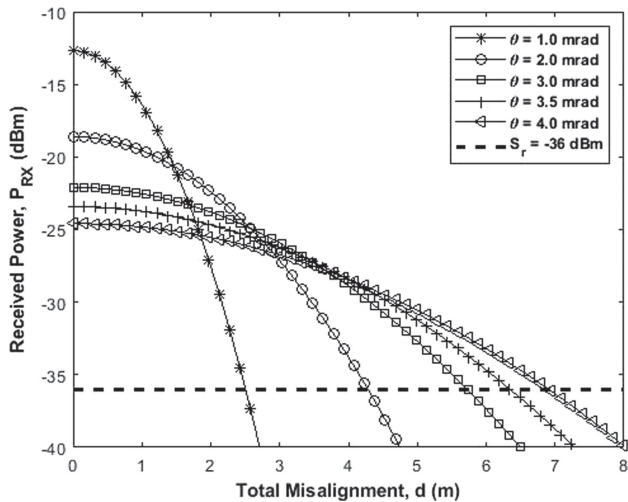


Fig. 7. Received power as a function of total misalignment for different divergence angles ( $L = 3$  km,  $\alpha_{\text{atm}} = 1$  dB/km).

Table 4. Maximum Misalignment ( $d_{\text{max}}$  in Meters) for Different Divergence Angles and Atmospheric Losses ( $L = 3$  km)

$\alpha_{\text{atm}}$ (dB/km)	$\theta$ (mrad)				
	1.0	2.0	3.0	3.5	4.0
1	2.503	4.279	5.758	6.345	6.792
2	2.337	3.894	5.105	5.535	5.888
3	2.123	3.328	4.232	4.533	4.683

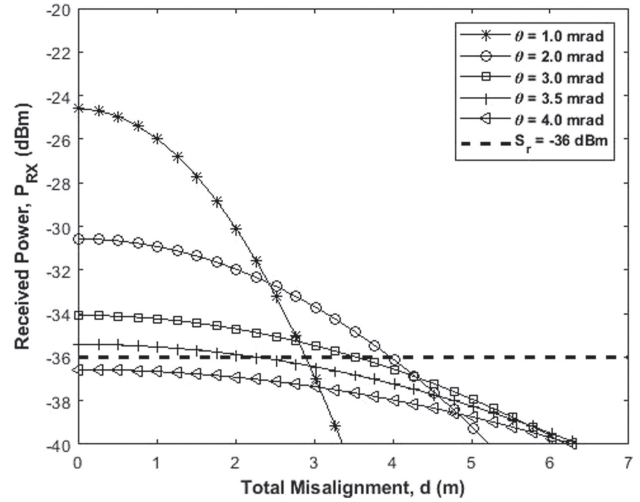


Fig. 8. Received power as a function of total misalignment for different divergence angles ( $L = 5$  km,  $\alpha_{\text{atm}} = 2$  dB/km).

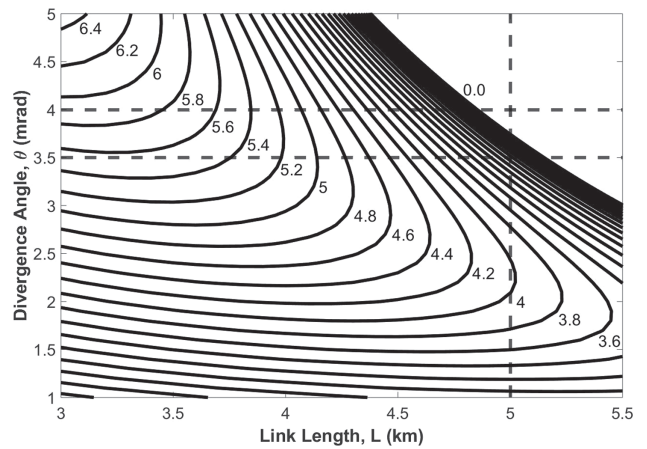
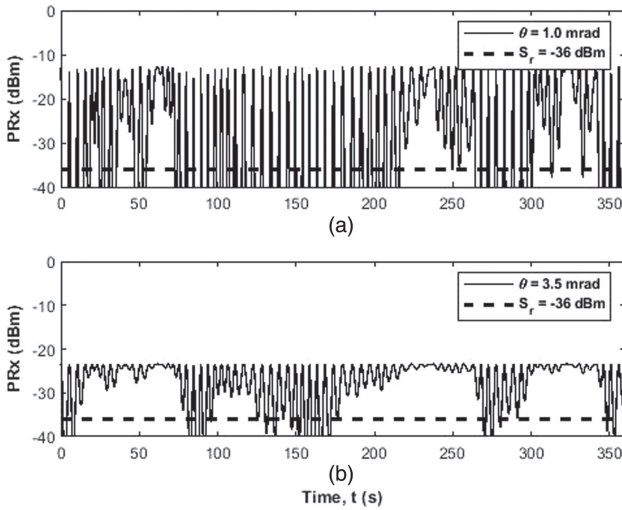


Fig. 9. Contour plot of  $d_{\text{max}}$  (m) as a function of link length and divergence angle ( $\alpha_{\text{atm}} = 2$  dB/km).

small values of  $d_{\text{max}}$  and, consequently, low probability of operating in shaky sea conditions.

In this work, the optimum divergence angle was analyzed in terms of  $d_{\text{max}}$ . This way, independently if the sea conditions generate high motion, the system was dimensioned with a divergence angle that optimizes the range of possible displacements and thus maximizes the link availability. Figure 9 shows the range of  $d_{\text{max}}$ , in the form of contour lines, within the operational range for  $\alpha_{\text{atm}} = 2$  dB/km. The blank area at the upper right corner represents the region where no



**Fig. 10.** Received power as a function of time for (a)  $\theta = 1$  mrad and (b)  $\theta = 3.5$  mrad. ( $L = 3$  km,  $\alpha_{\text{atm}} = 1$  dB/km).

misalignment is possible because it is at the right of the line where  $d_{\text{max}} = 0.0$  m. Hence, this figure also demonstrates that  $\theta = 4$  mrad is not a possible angle. Thus, we decided to choose  $\theta = 3.5$  mrad and privilege the link availability for  $L = 3$  km ( $d_{\text{max}} = 5.535$  m) in detriment of  $L = 5$  km ( $d_{\text{max}} = 2.271$  m). Another possible solution could be choosing  $\theta = 2$  mrad, where  $d_{\text{max}} \approx 4$  m for the entire range of link distances, but this choice would compromise the availability for  $\alpha_{\text{atm}} = 1$  dB/km.

The received optical power as a function of time is shown in Fig. 10. It is possible to observe that, for  $\theta = 1$  mrad, the power reaches the reception threshold more frequently than for  $\theta = 3.5$  mrad. Hence, the availability is higher, remaining above the sensitivity for longer periods, when  $\theta = 3.5$  mrad.

## 2. Link Length and Atmospheric Loss

Subsequently, considering  $\theta = 3.5$  mrad, the proposed model was simulated for different distances. Figure 11 shows these results. For  $L = 5$  km, the optical power drastically decreases, in comparison to 3 km, but remains above the reception threshold. In this case, the FSO system operates with  $d_{\text{max}} = 7.034$  m. When  $L > 7.5$  km, we observe that the received optical power remains below the reception threshold and the system becomes inoperative.

The same simulations were performed for  $\alpha_{\text{atm}} = 2$  and 3 dB/km. The results are presented in Fig. 12 and show that an increase in  $L$  and the consequent increase in atmospheric and scintillation losses considerably reduce the received power. In this case, when  $L = 5$  km, despite the reduction of  $d_{\text{max}}$  to 2.271 m, the FSO system can still operate for  $\alpha_{\text{atm}} = 2$  dB/km but becomes inoperative for  $\alpha_{\text{atm}} = 3$  dB/km.

These impacts were also perceived during the temporal analysis, shown in Fig. 13. When  $L = 3$  and 5 km, the FSO receives a maximum  $P_{\text{RX}}$  of  $-26.436$  and  $-35.418$  dBm, respectively.

Thus, through the analyses described in this section, it is possible to conclude that a divergence angle of 3.5 mrad was more suitable to compensate for the platform motions

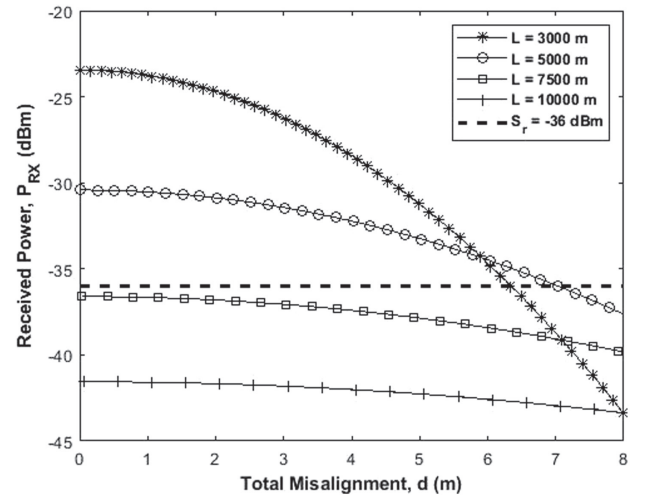


**Fig. 11.** Received power as a function of total misalignment for different distances ( $\theta = 3.5$  mrad,  $\alpha_{\text{atm}} = 1$  dB/km).

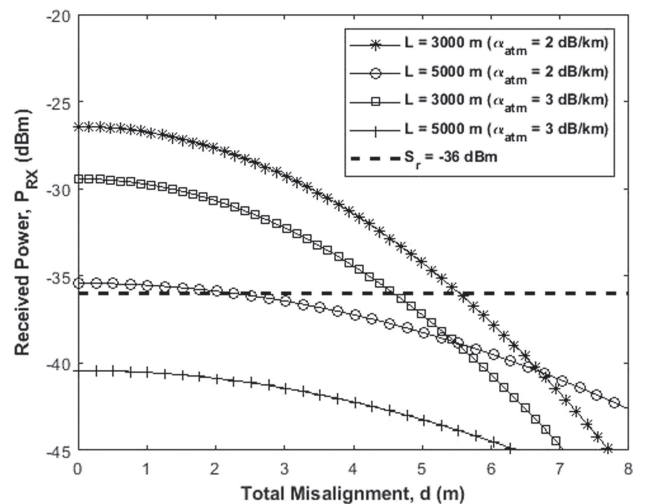


**Fig. 12.** Received power as a function of total misalignment for different distances ( $\theta = 3.5$  mrad,  $\alpha_{\text{atm}} = 2$  and 3 dB/km).

within the predefined operational range:  $3 \text{ km} \leq L \leq 5 \text{ km}$  and  $1 \text{ dB/km} \leq \alpha_{\text{atm}} \leq 2 \text{ dB/km}$ .

## C. Availability Analysis

In this subsection, the FSO system is analyzed in terms of availability. The influence of the wave parameters ( $H_s$  and  $T_p$ ) is also considered. As depicted in Subsection 2.C, the system availability rate was evaluated within the proposed operational range.

### 1. Availability Rates

As previously stated, the sea state ( $H_s = 0.25$  m,  $T_p = 11$  s,  $\chi = 135^\circ$ ) was chosen to evaluate the impact of a resonant state. Hence, the availability rates for this state are shown in Table 5. In this table, each result was calculated for the following conditions:  $\eta_1$  for  $L = 3$  km and  $\alpha_{\text{atm}} = 1$  dB/km,  $\eta_2$  for

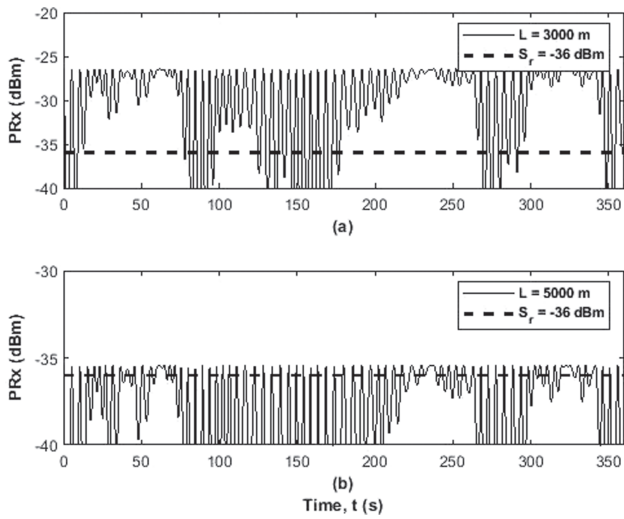


**Fig. 13.** Received power as a function of time for (a)  $L = 3$  km and (b)  $L = 5$  km ( $\theta = 3.5$  mrad,  $\alpha_{atm} = 2$  dB/km).

**Table 5. FSO System Availability ( $\eta$ )**

$\theta$ (mrad)	$\eta_1$ (%)	$\eta_2$ (%)	$\eta_3$ (%)	$\eta_4$ (%)
1.0	43.500	40.813	36.667	29.875
2.0	66.625	61.917	54.938	41.438
3.0	80.000	74.688	63.313	37.125
3.5	84.771	78.979	65.833	22.646
4.0	88.667	81.750	66.542	0.000

$L = 3$  km and  $\alpha_{atm} = 2$  dB/km,  $\eta_3$  for  $L = 5$  km and  $\alpha_{atm} = 1$  dB/km, and  $\eta_4$  for  $L = 5$  km and  $\alpha_{atm} = 2$  dB/km.

For  $L = 3$  km, it is noticed that the availability rates are higher for higher divergence angles. This behavior is also observed in the next two columns. However, when the FSO link reaches 5 km, under the influence of  $\alpha_{atm} = 2$  dB/km, the receiver operates so close to its sensitivity that the availability

becomes lower, until it reaches zero. Thus, to meet the operating conditions, divergence angles higher than 3.5 mrad are not recommendable.

Finally, the system availability rates were obtained for each pair of representative values ( $H_s, T_p$ ) and are shown in Table 1 for each one of the four wave incidence angles ( $\chi$ ). Thus, at the end of this process, 312 representations of the sea state were used. Tables 6 and 7 show the availability rates, averaged from the four wave incidences and calculated for  $L = 3$  km,  $\theta = 1$  mrad (Table 6), and  $\theta = 3.5$  mrad (Table 7).

### 2. Boresight Error

All results presented in the previous sections were obtained considering the sea motions as the influence of jitter on the pointing error. That is, initially, TX and RX were considered at a condition of link alignment. The impacts caused by the boresight error ( $\delta$ ) in the pointing of the FSO system were inserted as fixed displacements in the horizontal ( $x_c + \delta$ ) and vertical ( $y_c + \delta$ ) components of Eq. (6). Thus, an evaluation of the availability rate was made for the sea state ( $H_s = 0.25$  m,  $T_p = 11$  s,  $\chi = 135^\circ$ ) and different values of  $\delta$ , obtaining the results presented in Fig. 14.

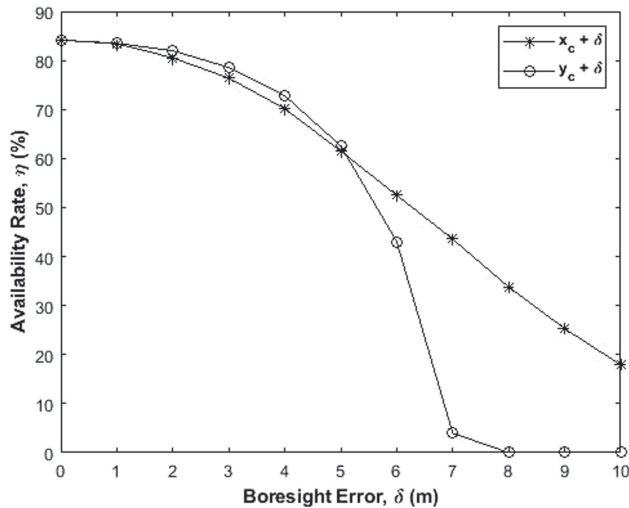
The curves in Fig. 14 show that, when  $\delta = 0$ , the availability rate is equal to 84.771%, the same result shown in Table 5. With increasing boresight errors, there is a continuous reduction in the system availability due to the increase in the values of  $\delta$ . When  $\delta = 5$  m, the difference between the two availabilities is quite small: 61.5% for the horizontal boresight error and 62.58% for the vertical one. However, for  $\delta = 6$  m, the boresight error starts to significantly influence the misalignment on the  $y$  axis, so that when  $\delta = 7$  m, there is an abrupt drop in the system availability rate (3.98%) and, when  $\delta = 8$  m, the link becomes inoperative. On the other hand, when  $\delta = 10$  m on the horizontal boresight error, the system operates with low availability (17.92%).

**Table 6. Scatter Diagram of Availability Rates ( $L = 3$  km,  $\theta = 1$  mrad)**

$H_s$ (m)	$T_p$ (s)							$H_{spr}$ (m)
	2-4	4-6	6-8	8-9	10-12	12-14	14-16	
7.5-8.0					2.000			7.75
7.0-7.5					2.182	2.302		7.25
6.5-7.0					2.401	2.537		6.75
6.0-6.5				3.141	2.719	2.891		6.25
5.5-6.0				3.526	3.136	3.250	4.490	5.75
5.0-5.5			3.370	3.880	3.641	3.698	5.047	5.25
4.5-5.0			6.250	4.448	4.235	4.313	5.844	4.75
4.0-4.5			7.125	5.224	4.938	5.115	6.922	4.25
3.5-4.0			8.110	6.005	5.885	6.235	8.255	3.75
3.0-3.5		35.167	9.469	7.094	7.068	7.630	9.891	3.25
2.5-3.0		41.682	11.422	8.547	8.542	9.531	12.047	2.75
2.0-2.5		50.156	14.443	10.688	10.792	12.078	15.047	2.25
1.5-2.0	100	61.761	18.787	13.948	14.037	15.839	19.568	1.75
1.0-1.5	100	77.255	26.188	19.578	19.417	22.417	26.698	1.25
0.5-1.0	100	96.866	42.417	31.584	30.599	33.693	37.938	0.75
0.0-0.5	100	100	88.860	69.438	59.849	61.328	65.953	0.25
$T_{pp}$ (s)	3	5	7	9	11	13	15	-

**Table 7. Scatter Diagram of Availability Rates ( $L = 3$  km,  $\theta = 3.5$  mrad)**

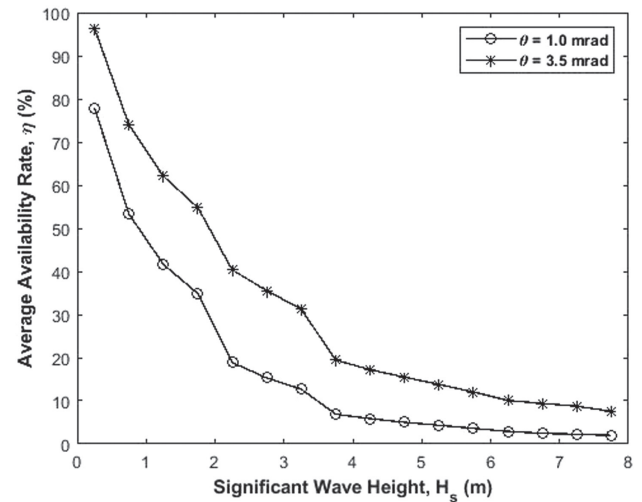
$H_s$ (m)	$T_p$ (s)							$H_{spp}$ (m)
	2-4	4-6	6-8	8-10	10-12	12-14	14-16	
7.5-8.0					7.589			7.75
7.0-7.5					8.325	9.151		7.25
6.5-7.0					8.907	9.880		6.75
6.0-6.5				9.703	9.719	10.844		6.25
5.5-6.0				10.604	10.714	11.948	14.896	5.75
5.0-5.5			15.855	11.714	11.750	13.219	16.474	5.25
4.5-5.0			17.625	13.787	12.943	14.761	18.302	4.75
4.0-4.5			19.740	14.579	14.625	16.656	20.427	4.25
3.5-4.0			22.250	16.589	16.547	18.870	23.073	3.75
3.0-3.5		76.042	25.484	19.110	18.990	21.792	26.130	3.25
2.5-3.0		83.354	29.964	22.209	22.266	25.370	30.120	2.75
2.0-2.5		88.110	36.073	26.985	26.526	29.969	34.360	2.25
1.5-2.0	100	96.391	45.724	33.682	32.637	35.688	39.557	1.75
1.0-1.5	100	99.271	60.021	44.526	40.984	43.568	46.122	1.25
0.5-1.0	100	100	83.219	63.407	54.943	56.119	60.141	0.75
0.0-0.5	100	100	99.719	95.891	91.624	92.391	95.542	0.25
$T_{pp}$ (s)	3	5	7	9	11	13	15	-

**Fig. 14.** Boresight error analysis ( $H_s = 0.25$  m,  $T_p = 11$  s,  $\chi = 135^\circ$ ,  $L = 3$  km,  $\theta = 3.5$  mrad,  $\alpha_{atm} = 1$  dB/km).

This abrupt drop in performance caused by the increase in boresight error on the vertical axis is due to impacts caused by the resonance peak of the pitch movement observed at  $T_p = 11$  s. For this same  $T_p$ , it is observed that the resonance peak of the yaw rotation is lower, making the boresight error less impactful on the horizontal axis compared to the vertical axis. In addition, an error of  $\delta = 6$  m is very near the maximum displacement observed for this configuration in Table 4 ( $d_{max} = 6.345$  m).

### 3. Significant Wave Height

Figure 15 shows the availability of the system as a function of  $H_s$ . The results were obtained by averaging each line in Tables 6 and 7. As expected, it can be seen that the availability decreases due to the increase in wave heights. Furthermore, the

**Fig. 15.** Average availability as a function of significant wave height.

curves show that this reduction occurs in a similar way for the two systems, the availability being higher for  $\theta = 3.5$  mrad.

### 4. Peak Period

Similar to the analysis made for  $H_s$ , the average availability as a function of peak period ( $T_p$ ) was calculated and its values are represented in Fig. 16.

The curves show a similar behavior regarding the analyzed peak periods. For both values of  $\theta$ , the availability rates decrease rapidly up to  $T_p = 11$  s, when they start to slightly increase again. In this case, it is possible to conclude that the variations in the availability rates observed in Fig. 16 follow the hydrodynamic behavior of the vessel. This happens especially in the presence of motions that create resonating frequencies, such as those described by the pitch and yaw RAO curves, for  $\chi = 135^\circ$  [see Figs. 5(e) and 5(f)]. Therefore, the availability

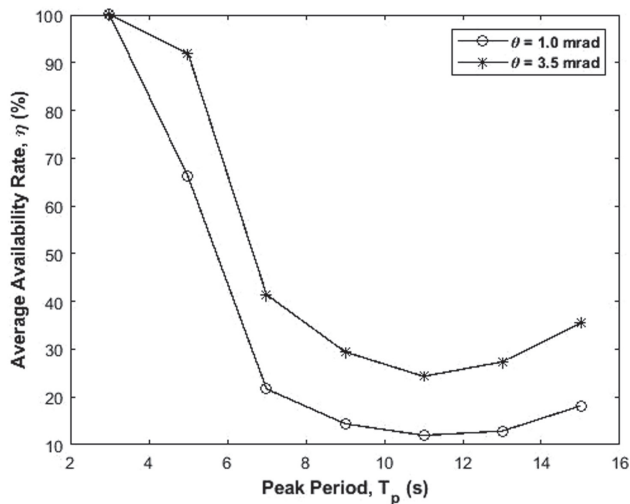


Fig. 16. Average availability as a function of the peak period.

of the FSO system on board the Mariner can be described by the RAO curves that most affect the stability of the maritime platform.

### 5. Expected Data Rates

As previously said, the proposed system posses a beacon laser, on another wavelength, which signalizes if the link is ready to transmit. This way, it is capable of detecting the uptime windows, such as those presented in Figs. 10 and 13, and immediately transmit data at full rate. Hence, considering that the communication link has a bit rate of 1 Gbps, due to the succession of up and downtime windows of availability, in a long time, the link presents an effective data rate given by the availability rate multiplied by the bit rate.

In order to know which data rate to expect in such random conditions as the sea, the availability rates of Tables 6 and 7 were divided into ranges of 5% and the probability of occurrence of each range was calculated based on Table 1. Figure 17

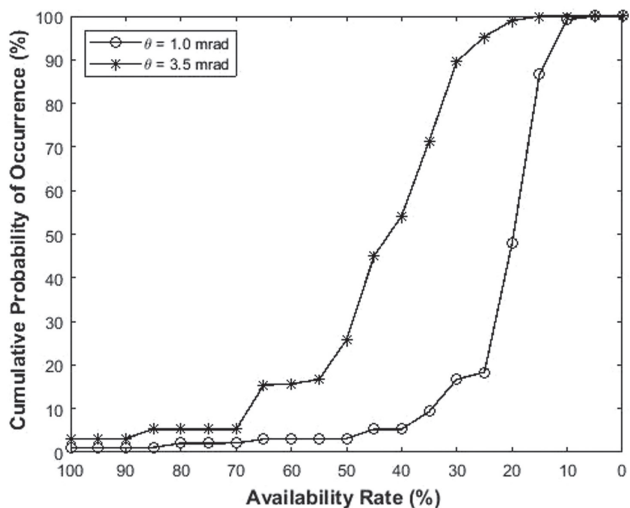


Fig. 17. Cumulative probability of occurrence as a function of availability rate ranges.

shows the cumulative probability of occurrence for each availability rate range. The availability rate axis was purposely inverted to show the probability of high data rates first.

The curves show that the system has a low probability of operating with an availability above 70% (5.3% for 3.5 mrad, and 2.1% for 1 mrad). This availability corresponds to an effective data rate of 700 Mbps. Later, it is observed that the probability of the system to operate above 500 Mbps increases to 25.8% for 3.5 mrad, but it remains practically unchanged (3.2%) for 1 mrad. Finally, with 90% of confidence, the system operates at an effective rate of 300 Mbps and 136.6 Mbps, for each one of the analyzed divergence angles.

### 4. CONCLUSION

In this work, the availability of an FSO communication link established between a maritime platform and a land base was analyzed. To achieve this goal, the hydrodynamic system was modeled to determine the most appropriate angle of divergence (3.5 mrad) to compensate for geometric and misalignment losses in given operational conditions.

Despite the dependence of hull geometry and sea conditions, the presented methodology is applicable to any maritime platform. Thus it was demonstrated that, for the considered FSO and vessel alignment, pitch and yaw rotations have a great impact on the misalignment of the link. An analysis based on RAO curves was done and showed its relation to the behavior of the communication system. The use of Marcum's  $Q$  function is suitable for this kind of application, which involves several sea states, as it is rapidly processed.

The optical subsystem was analyzed in terms of divergence angle, link length, and atmospheric attenuation. Through this analysis, it was possible to conclude that a divergence angle of 3.5 mrad was more suitable to compensate for the platform motions, within the predefined operational lengths: 3 km to 5 km. The proposed FSO system was designed to operate under conditions of clean weather and fine fog. This corresponds to an operational range of  $\alpha_{atm}$  between 1 dB/km and 2 dB/km. Nevertheless, the system can still work for higher values of  $\alpha_{atm}$ , such as 3 dB/km, if the ship's distance to the coast is near 3 km.

In addition, the FSO system availability was analyzed in terms of boresight error, significant wave height, and peak period of the sea spectrum. It was noted that boresight errors above 5 m can reduce drastically the system performance, especially for the vertical axis. Regarding the sea conditions, it is possible to conclude that the availability decreases due to the increase in wave heights or in the presence of motions that create resonating states on the vessel.

The operation at an effective data rate of 300 Mbps, in 90% of the observed sea conditions, was demonstrated when using a beacon system as PAT. Higher data rates, such as 400 Mbps, are also possible although less probable ( $\leq 50\%$ ). Therefore, the methodology developed in this article can be used to optimize the availability of FSO links implemented on offshore platforms under the influence of ocean wave motions. In another perspective, this methodology can be applied to reduce costs in measuring the motions of hydrodynamic systems in a controlled environment.

## REFERENCES

- W. S. Rabinovich, C. I. Moore, R. Mahon, P. G. Goetz, H. R. Burris, M. S. Ferraro, J. L. Murphy, L. M. Thomas, G. C. Gilbreath, M. Vilcheck, and M. R. Suite, "Free-space optical communications research and demonstrations at the US Naval Research Laboratory," *Appl. Opt.* **54**, F189–F200 (2015).
- V. G. A. Carneiro, G. K. Rodrigues, and M. T. M. R. Giraldi, "Simulation of a temporal hard-limited OCDMA system over FSO link under average turbulence," *J. Microw. Optoelectron. Electromagn. Appl.* **12**, 79–95 (2013).
- M. A. Khalighi and M. Uysal, "Survey on free space optical communication: a communication theory perspective," *IEEE Commun. Surv. Tutorials* **16**, 2231–2258 (2014).
- H. Kaushal, V. Jain, and S. Kar, *Free Space Optical Communication, Optical Networks* (Springer, 2017).
- G. K. Rodrigues, V. G. A. Carneiro, A. R. da Cruz, and M. T. M. Giraldi, "Evaluation of the strong turbulence impact over free-space optical links," *Opt. Commun.* **305**, 42–47 (2013).
- W. S. Rabinovich, C. I. Moore, H. R. Burris, J. L. Murphy, M. R. Suite, R. Mahon, M. S. Ferraro, P. G. Goetz, L. M. Thomas, C. Font, G. C. Gilbreath, B. Xu, S. Binari, K. Hacker, S. Reese, W. T. Freeman, S. Frawley, E. Saint-Georges, S. Uecke, and J. Sender, "Free space optical communications research at the U.S. Naval Research Laboratory," *Proc. SPIE* **7587**, 758702 (2010).
- H. Kaushal and G. Kaddoum, "Applications of lasers for tactical military operations," *IEEE Access* **5**, 20736–20753 (2017).
- S. Fathi-Kazerooni, Y. Kaymak, R. Rojas-Cessa, J. H. Feng, N. Ansari, M. C. Zhou, and T. R. Zhang, "Optimal positioning of ground base stations in free-space optical communications for high-speed trains," *IEEE Trans. Intell. Transp. Syst.* **19**, 1940–1949 (2018).
- X. Chen, J. Ding, H. Lai, and S. Fathi-Kazerooni, "Performance analysis of free space optical communication systems for high-speed trains," *IET Optoelectron.* **1447**, 1–6 (2019).
- Q. Fan, M. Taheri, N. Ansari, J. Feng, R. Rojas-Cessa, M. C. Zhou, and T. Zhang, "Reducing the impact of handovers in ground-to-train free space optical communications," *IEEE Trans. Veh. Technol.* **67**, 1292–1301 (2018).
- H. S. Khallaf and M. Uysal, "UAV-based FSO communications for high speed train backhauling," in *IEEE Wireless Communications and Networking Conference (WCNC)*, 1–6 April 2019.
- Y. Kaymak, R. Rojas-Cessa, J. Feng, N. Ansari, M. Zhou, and T. Zhang, "A survey on acquisition, tracking, and pointing mechanisms for mobile free-space optical communications," *IEEE Commun. Surv. Tutorials* **20**, 1104–1123 (2018).
- J. C. Juarez, A. Dwivedi, A. R. Hammons, S. D. Jones, V. Weerackody, and R. A. Nichols, "Free-space optical communications for next-generation military networks," *IEEE Commun. Mag.* **44**(11), 46–51 (2006).
- F. Yang, J. Cheng, and T. A. Tsiftsis, "Free-space optical communication with nonzero boresight pointing errors," *IEEE Trans. Commun.* **62**, 713–725 (2014).
- M. Chen, "Robust tracking control for self-balancing mobile robots using disturbance observer," *IEEE/CAA J. Automat. Sin.* **4**, 458–465 (2017).
- S. Bloom, E. Korevaar, and J. Schuster, "Understanding the performance of free-space optics [Invited]," *J. Opt. Netw.* **2**, 178–200 (2003).
- I. I. Kim and E. J. Korevaar, "Availability of free-space optics (FSO) and hybrid FSO/RF systems," *Proc. SPIE* **4530**, 84–95 (2001).
- A. Prokes, "Atmospheric effects on availability of free space optics systems," *Opt. Eng.* **48**, 066001 (2009).
- J. Turán and L. Ovsenik, "Experimental FSO network availability estimation using interactive fog condition monitoring," *Proc. SPIE* **10142**, 1014223 (2016).
- A. A. Basahel, M. R. Islam, S. A. Zabidi, and M. H. Habaebi, "Availability assessment of free-space-optics links with rain data from tropical climates," *J. Lightwave Technol.* **35**, 4282–4288 (2017).
- V. V. Mai and H. Kim, "Link availability of airborne free-space optical communication systems under effect of generalized misalignment," in *23rd Opto-Electronics and Communications Conference (OECC)* (2018).
- S. Chandrasekaran, *Dynamic Analysis and Design of Offshore Structures*, 2nd ed. (Springer, 2018).
- Y. Bai and W. L. Jin, *Marine Structural Design*, 2nd ed. (Elsevier, 2016).
- W. Journée and J. M. J. Massie, *Offshore Hydromechanics*, 1st ed. (Delft University of Technology, 2001).
- National Maritime Research Institute (NRMI), "Global winds and waves," 2006, [https://www.nmri.go.jp/study/Intellectual/globus/11/32-ann10yrs-hp\\_e.html](https://www.nmri.go.jp/study/Intellectual/globus/11/32-ann10yrs-hp_e.html).
- K. Hasselmann, T. Barnett, and E. Bouws, *Measurements of Wind-Wave Growth and Swell Decay During the Joint North Sea Wave Project (JONSWAP)* (Deutsches Hydrographisches Institut, 1973).
- L. Roncetti, F. N. Corrêa, C. H. Albrecht, and B. P. Jacob, *Development of Operational Limit Diagrams for Offshore Lifting Procedures* (2015).
- B. P. Jacob, R. de Almeida Bahiense, F. N. Correa, and B. M. Jacovazzo, "Parallel implementations of coupled formulations for the analysis of floating production systems, part I: coupling formulations," *Ocean Eng.* **55**, 206–218 (2012).
- R. B. Zubaly, *Applied Naval Architecture* (Schiffer, 2015).
- W. Meyers, D. Sheridan, and N. Salvessen, *NSRDC Ship-Motion and Sea-Load Computer Program Manual* (1975).
- C. A. R. Castillo, "Sobre a dinâmica não linear do balanço paramétrico," Ph.D. thesis (Universidade Federal do Rio de Janeiro, 2009).
- N. Salvessen, E. Tuck, and O. Faltinsen, "Ship motions and sea loads," *Soc. Nav. Archit. Mar. Eng. Trans.* **78**, 250–287 (1970).
- M. St. Denis and W. J. Pierson, "On the motions of ships in confused seas," *Soc. Naval Archit. Maritime Eng. Trans.* **61**, 81 (1953).
- P. Brodtkorb, P. Johannesson, G. Lindgren, I. Rychlik, J. Rydén, and E. Sjö, "WAFO—a Matlab toolbox for the analysis of random waves and loads," in *Tenth International Offshore and Polar Engineering Conference (ISOPE)*, Seattle (2000), pp. 343–350.
- A. Siegman, "Unstable optical resonators for laser applications," *Proc. IEEE* **53**, 277–287 (1965).
- H. Kogelnik and T. Li, "Laser beams and resonators," *Appl. Opt.* **5**, 1550–1567 (1966).
- T. S. Khwaja and S. A. Reza, "Low-cost Gaussian beam profiling with circular irises and apertures," *Appl. Opt.* **58**, 1048–1056 (2019).
- C. P. Azzolin, A. F. Gurgel, and V. G. A. Carneiro, "Marcum Q-function as an analytical solution for misaligned Gaussian beams," *Opt. Eng.* **60**, 056105 (2021).
- L. C. Andrews, R. L. Phillips, C. Y. Hopen, and M. A. Al-Habash, "Theory of optical scintillation," *J. Opt. Soc. Am. A* **16**, 1417–1429 (1999).
- L. Dordová and O. Wilfert, "Calculation and comparison of turbulence attenuation by different methods," *Radioengineering* **19**, 162–167 (2010).
- J. A. H. Osorio, "Simulação e desenvolvimento de um enlace de free-space optics no Rio de Janeiro e a relação com a ITU-T G.826," Ph.D. thesis (Pontifícia Universidade Católica do Rio de Janeiro, 2005).
- I. I. Kim, R. Stieger, J. Koontz, C. Moursund, M. Barclay, P. Adhikari, J. J. Schuster, E. J. Korevaar, R. Ruigrok, and C. M. DeCusatis, "Wireless optical transmission of fast ethernet, FDDI, ATM, and ESCON protocol data using the TerraLink laser communication system," *Opt. Eng.* **37**, 3143–3155 (1998).
- V. G. A. Carneiro, G. K. Rodrigues, and M. T. M. R. Giraldi, "Performance analysis of a 2D double hard-limited OCDMA system over FSO link under strong turbulence for defense applications," in *MILCOM 2012–2012 IEEE Military Communications Conference (IEEE, 2012)*.
- A. Touati, A. Abdaoui, F. Touati, M. Uysal, and A. Bouallegue, "On the effects of combined atmospheric fading and misalignment on the hybrid FSO/RF transmission," *J. Opt. Commun. Netw.* **8**, 715–725 (2016).
- Instituto Nacional de Meteorologia (INMET), "Meteorological database," 2021, <https://bdmep.inmet.gov.br/>